Exclusive Co-N_4 Sites Confined in Two-dimensional Metal-Organic Layers Enabling Highly Selective CO_2 Electroreduction at Industrial-Level Current

Dr. Wenjun Zhang, Dr. Shanshan Liu, Dr. Yue Yang, Dr. Haifeng Qi, Dr. Shibo Xi, Dr. Yanping Wei, Dr. Jie Ding, Prof. Zhu-Jun Wang, Prof. Qunxiang Li*, Prof. Bin Liu*, Prof. Zupeng Chen*

Abstract

Metal-organic framework catalysts bring new opportunities for CO_2 electrocatalysis. Herein, we first conduct density-functional theory calculations and predict that Co-based porphyrin porous organic layers (Co-PPOLs) exhibit good activity for CO_2 conversion because of the low *CO adsorption energy at Co-N_4 sites, which facilitates *CO desorption and CO formation. Then, we prepare two-dimensional Co-PPOLs with exclusive Co-N_4 sites through a facile surfactant-assisted bottom-up method. The ultrathin feature ensures the exposure of catalytic centers. Together with large specific area, high electrical conductivity and CO_2 adsorption capability, Co-PPOLs achieve a peak faradaic efficiency for CO production (FE_{CO}=94.2 %) at a moderate potential in CO_2 electroreduction, accompanied with good stability. Moreover, Co-PPOLs reach an industrial-level current above 200 mA in a membrane electrode assembly reactor, and maintain near-unity CO selectivity (FE_{CO}>90 %) over 20 h in CO_2 electrolysis.

Introduction

Excessive CO_2 emissions have caused serious environmental problems, especially global warming and ocean acidification. Upgrading CO_2 into high-value-added chemicals and fuels is anticipated to alleviate the aforementioned issues and realize carbon neutrality. Electrocatalytic CO_2 reduction reaction (CO_2RR) is regarded as one of the most promising strategies that can effectively convert CO_2 into value-added products (e.g., CO, formate, CH_4, hydrocarbons, and oxygenates), of which CO is an important feedstock to produce olefins through Fischer–Tropsch technology.[1] Among the developed library of catalysts, metal single atoms anchored on N-doped carbon materials (M-SAs/NC) have exhibited satisfying catalytic activity for the selective electrocatalytic CO_2-to-CO conversion, and the atomically dispersed metal coordinated with N species (M-N_x) were considered to be the active sites.[2] However, the difficulties in controllable synthesis and the non-uniform structure in the carbon matrix impose challenges in confirming the real active centers and catalytic mechanisms. Therefore, designing novel electrocatalysts with well-defined catalytic sites is highly desired.

Metal-organic frameworks (MOFs), a class of newly developed porous materials, can confine atomically dispersed metal sites in highly ordered crystalline structures.[3] Due to the long-range order with periodic structures and the presence of well-isolated metal sites, MOFs find promising applications in gas adsorption, catalysis, electrochemical energy conversion, etc.[4] In natural photosynthesis, a self-assembled structure of

chlorophyll (i.e., magnesium-containing porphyrin organic framework) plays a vital role in the process of CO_2 fixation/activation.[5] This kind of porphyrin-based MOF has a well-defined Mg-N_4 coordination structure, which can act as a model catalyst to provide the active sites and study the catalytic mechanism for CO_2RR. Moreover, porphyrin-based MOFs are a category of potential electrocatalysts because of their low cost, accessibility, and high chemical stability. In addition, their catalytic activities and selectivities can be adjusted by tuning the metal centers or the macrocyclic ligands.[6] For example, a Co protoporphyrin immobilized on a pyrolytic graphite electrode reached a faradaic efficiency for CO production (FE_{CO}) over 60 % at a relatively low overpotential of 0.5 V.[7] In another e, a covalent organic framework catalyst comprising Co porphyrin units exhibited high FE_{CO} of 90 % at an overpotential of 0.55 V.[8] A Fe-tetraphenylporphyrin catalyst modified by phenolic groups sped up CO_2RR, which manifested a FE_{CO} above 90 % over 4 h electrolysis at a low overpotential of 0.465 V.[9] Thus, the rational design of novel metal-complex building units is crucial in the functionalization of porphyrin-based MOFs for highly-efficient electrocatalytic CO_2RR. Nevertheless, the electrically insulating property of pristine MOFs suppresses efficient electron transfer to the inner surface, disabling a great number of the active sites, and finally leads to inferior electrocatalytic activity. Meanwhile, the conjugated planar structures readily agglomerate via intermolecular π-π stacking to form particles, which might influence the electrocatalytic stability.[10] Therefore, constructing porous low-dimensional frameworks to expose abundant active sites for high-performance CO_2RR without sacrificing the structural flexibility is intriguing, but challenging.

Since the discovery of graphene, numerous research work to develop novel two-dimensional (2D) materials have sprung up, such as graphene oxide,[11] MXene,[12] boron nitride,[13] conjugated polymers,[14] etc. Due to the ultrathin nanostructures and fascinating properties, these 2D materials show super performances in electrochemistry. Accordingly, constructing 2D metal-organic layers (MOLs) instead of three-dimensional (3D) MOFs can enable active atoms to be fully exposed,[15] and the periodic arrangement of organic units can also ensure structural homogeneity. The perfect crystallinity, large surface area, and high porosity are conducive to gas adsorption and charge transfer. Moreover, the stacking effect of 2D MOLs results in the difference in the atomic layer number, and distinct electronic and/or geometric configuration.[16] These properties can significantly regulate the pathways and activity of electrochemical CO_2RR. More importantly, compared to conventional single-atom sites supported on oxide or carbon nanolayers, MOLs comprising metal atoms bridged by organic ligands have well-defined active sites, which can serve as ideal models to explore the structure-function relationship. However, the molecular building blocks of layered bulk MOFs are interconnected through strong coordination bonds, which remains a significant challenge to directly obtain well-dispersed ultrathin MOLs. Accordingly, the top-down method has been widely used to synthesize 2D MOLs through sonication or shaking

operations, aiming at breaking the weak inter-layer interactions (e.g., van der Waals forces or hydrogen bonding).[17] Nevertheless, this method is not feasible for the uniform and large-scale synthesis of MOLs, and the as-obtained MOLs are unstable owing to the tendency of restacking. Therefore, the rational design of novel MOL catalysts with proper coordination structure and abundant active sites through an advisable synthetic method is desired for highly-efficient electrocatalytic CO_2RR.

Herein, we first performed density-functional theory (DFT) calculations for porphyrin porous organic layers (PPOLs) with different metal centers, which identified Co-based PPOLs as the optimal catalyst for electrochemical CO_2RR due to the strong *COOH binding energy and moderate *CO adsorption at the Co-N_4 sites. To assess our theoretical predictions, metal porphyrin-based porous organic layers (M-PPOLs) with different metal centers (M=Co, Ni, and Fe) were directly prepared through a facile surfactant-assisted bottom-up synthetic method and evaluated in the electrocatalytic CO_2RR. Different from the traditional top-down exfoliation method, the bottom-up method not only contributes to the anisotropic growth of MOFs and the formation of ultrathin MOLs, but also facilitates the high-yield preparation of catalysts. The as-synthesized ultrathin morphology with a thickness of sub-5 nm ensured the exposure of abundant active atoms, which synergistically improved the surface area, electrical conductivity, and CO_2 adsorption capability. In addition, as an ideal single-site catalyst, Co porphyrin-based porous organic layers (Co-PPOLs) possessed well-defined Co-N_4 sites and structural homogeneity. Thus-obtained Co-PPOLs catalyst realized optimal activity and selectivity for CO production (FE_{CO}=94.2 %) at a moderate potential (−0.9 V vs. RHE) during long-term CO_2 electrolysis. Furthermore, Co-PPOLs could reach an industrial-level current over 200 mA in a membrane electrode assembly (MEA) device, and realize the maximum FE_{CO} above 90 % up to 20 h. This work provides an inspiration to produce CO at a commercial scale with molecularly dispersed MOFs catalysts in a scale-up MEA reactor.

Results and Discussion

The electron density of Co-PPOLs was calculated by DFT and the results are displayed in Figure 1a. Clearly, the organic ligands with strong π-π orbital conjugation properties can provide high charge density and mobility for Co-PPOLs, which will effectively enhance their electronic conductivity due to the orbital overlap. The intermediate structures adsorbed on the Co-N_4 site during electrochemical CO_2-to-CO conversion are illustrated in Figure 1b. The DFT-calculated free-energy pathways on different M-PPOLs are presented in Figure 1c. As observed from the elementary reaction steps, *COOH formation is exergonic on Co-PPOLs (−0.33 eV), but is exothermic on both Ni-PPOLs (+1.00 eV) and Fe-PPPOLs (+0.06 eV), suggesting the better intrinsic CO_2RR activity of Co-PPOLs. Moreover, *CO desorption is regarded as the rate-determining step of CO_2RR on Co- and Fe-PPOLs due to the endothermic process, which plays a vital role in CO

formation. The desorption barrier of *CO to CO(g) over Co-PPOLs is +0.86 eV, which is much lower than that over Fe-PPOLs (+1.53 eV), indicating higher CO selectivity on the Co-N_4 site. Some previous studies have shown that covalent bonds can be roughly known from the hybridization of peaks in the projected density of states (PDOS), where large resonances of two peaks of different orbitals in the same energy region indicate strong bonds.[18] Accordingly, the electronic structures of *CO and *COOH adsorbed on different M-PPOLs have also been calculated (Figure 1d and 1e), among which, the electronic states of *CO in Co-PPOLs have a smaller resonance at the lowest energy below the Fermi level, indicating a weaker binding ability compared to the Fe-PPOLs. Furthermore, the d orbital of Co-PPOL has a larger resonance with *COOH below the Fermi level than that of Ni-PPOL. This indicates that Co-PPOL has a stronger bonding ability with *COOH than Ni-PPOL. Therefore, the DFT calculations demonstrate that Co-PPOLs are anticipated to exhibit the best intrinsic activity and selectivity for CO formation in CO_2 electrolysis. The mechanistic Scheme for the electrochemical CO_2-to-CO conversion on Co-PPOLs is proposed in Figure 1f. When the Co-PPOLs catalyst captures an electron, Co^{II} center is first reduced to Co^{I}, which has been proved by previous electrochemical studies.[19] We observe a similar behavior for the Co-PPOLs in the cyclic voltammetry (CV) test (Figure S1), where a broad reduction wave (1) at approximately −0.3 V (vs. RHE) assignable to the reduction of Co^{II} center to Co^{I} can be clearly identified during the electrochemical process. Subsequently, the CO_2 molecule adsorbs onto the Co^{I} species to form the Co^{II}-*COOH intermediate accompanied by the proton transfer. Afterwards, coupled with successive proton-electron transfer, Co^{II}-*COOH converts to Co^{I}-*CO intermediate, and finally releases gaseous CO via *CO desorption.

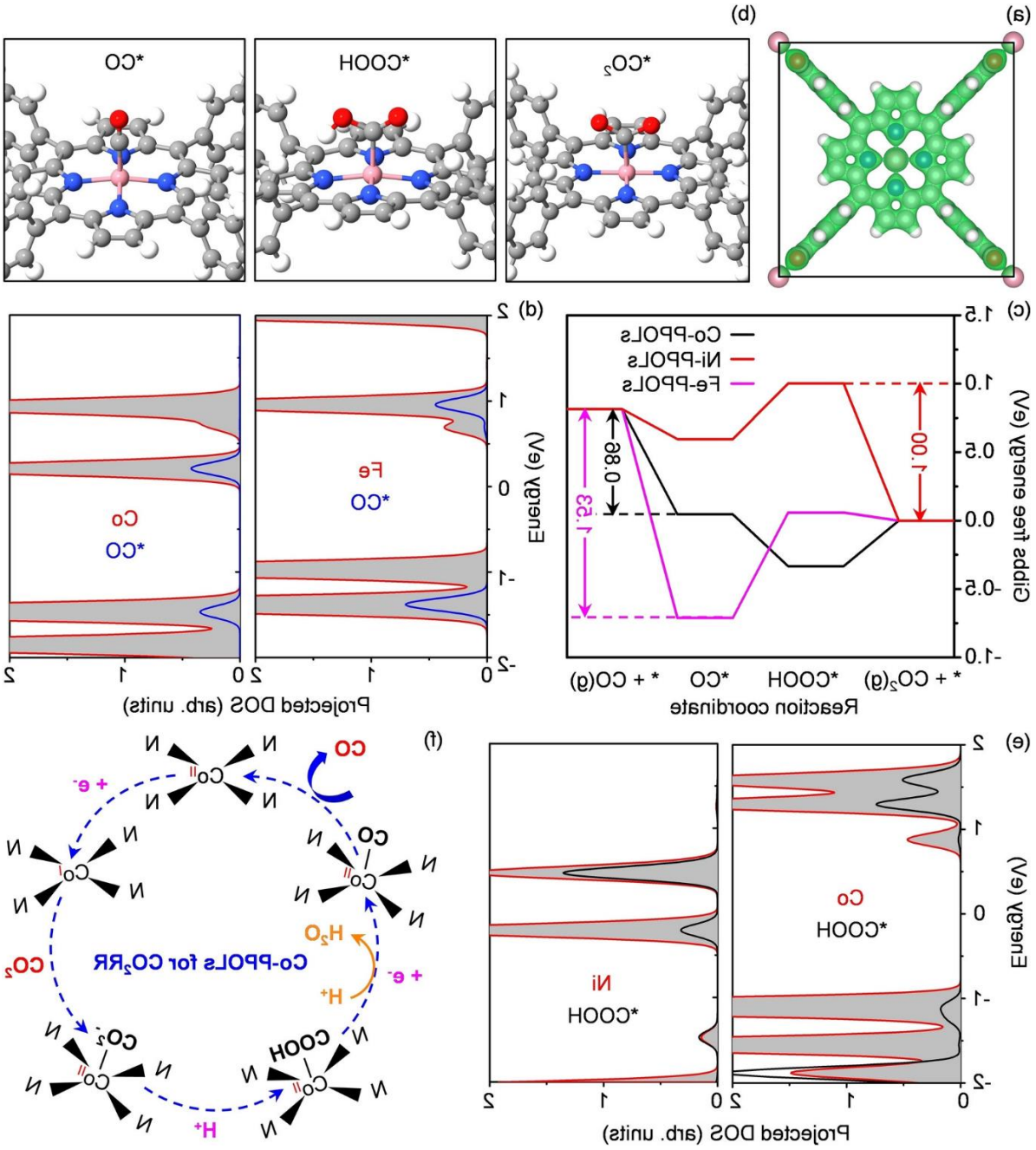

Figure 1 a) Electron density diagram of single-cell Co-PPOLs. b) The schematic diagrams of adsorbed *CO_2, *COOH, and *CO on Co-N_4 sites of Co-PPOLs. Co (pink), N (blue), C (gray), O (red), and H (white). c) Gibbs free energy diagrams for electrochemical CO_2-to-CO conversion. PDOS of the pristine structures from d) *CO and e) *COOH adsorption on different M-PPOLs (M=Co, Ni, and Fe). f) Proposed mechanistic scheme for the electrochemical CO_2-to-CO conversion on Co-PPOLs.

The freestanding 2D Co-PPOLs were synthesized through a surfactant-assisted synthesis approach at 80 °C using tetrakis(4-carboxyphenyl)-porphyrin (TCPP) and $Co(NO_3)_2{\cdot}6\,H_2O$ as the precursors (Co-PPOLs-80, Figure 2a). During the reaction, the TCPP ligand is coordinated by the Co^{2+} core. Then, four TCPP ligands linked with one $Co_2(COO)_4$ paddlewheel metal node and then crosslinked with each other to form a 2D

layered MOF structure.[17] Meanwhile, the surfactant attached to the surface of MOFs could stabilize the layers and restrict their growth along the vertical direction, thus leading to the anisotropic growth of MOFs and the formation of ultrathin 2D Co-PPOLs. Despite the high cobalt content (10.3 wt %, measured by inductively coupled plasma optical emission spectrometry, ICP-OES), no Co clusters or particles can be found on the surface based on integrated microscopic analyses (see below). The resulting Co-PPOLs-80 presents crumpled and wrinkled morphology, as revealed by transmission electron microscopy (TEM) (Figure 2b). The atomically dispersed Co sites were evidenced by the aberration-corrected high-angle annular dark-field scanning TEM (HAADF-STEM), showing numerous bright dots on the low-atomic number hosts (Figure 2c). The average thickness of Co-PPOLs-80 was determined to be ca. 3.8 nm by atomic force microscope (AFM) (Figure 2d), further demonstrating the 2D ultrathin feature. The use of surfactant (polyvinylpyrrolidone, PVP) not only contributes to the anisotropic growth of MOFs, but also facilitates the high-yield preparation of ultrathin MOLs, in contrast to the bulk form of MOF prepared via the traditional synthetic method without surfactant.[20] As shown in the HAADF-STEM image and the corresponding energy dispersive X-ray (EDX) elemental mappings (Figure 2e and f), C, N, O, and Co elements were revealed to be homogeneously distributed throughout Co-PPOLs-80.

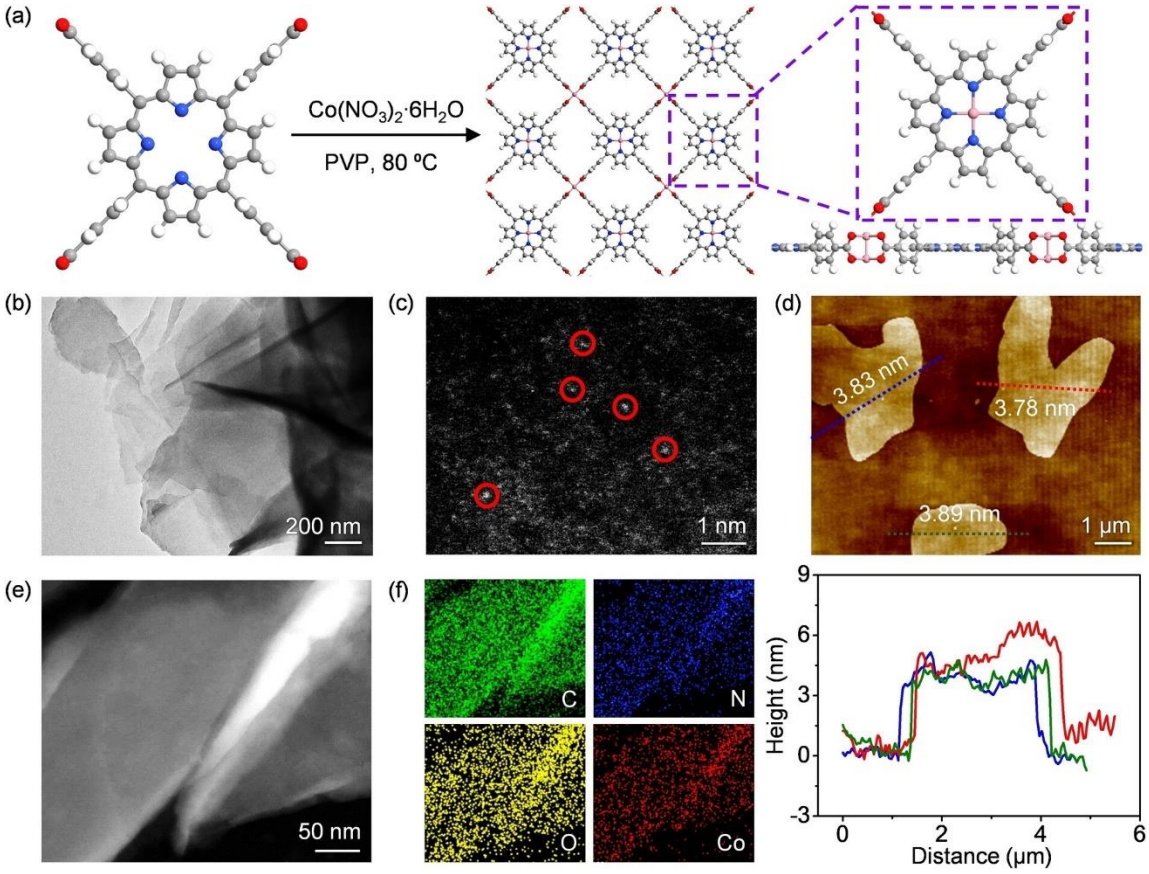

Figure 2 a) Schematic illustration of the synthesis of ultrathin 2D Co-PPOLs-80. Co (pink), N (blue), C (gray), O (red), and H (white). b) TEM and c) AC HAADF-STEM images of Co-PPOLs-80. d) AFM image (upper) and the corresponding height profiles (lower) of Co-

PPOLs-80. e) HAADF-STEM image and f) the corresponding elemental EDX mappings of Co-PPOLs-80.

To further confirm the precise structure of Co-PPOLs-80, X-ray absorption near edge structure (XANES) and extended X-ray absorption fine structure (EXAFS) spectroscopies were conducted. The normalized Co *K*-edge XANES spectra show that the absorption edge of Co-PPOLs-80 has an obvious shift toward the high energy region compared with Co foil and is close to CoO (Figure 3a), indicating that the Co atoms in Co-PPOLs-80 possess positive charge with valence state close to +2. The corresponding Fourier transform (FT) EXAFS spectrum of Co-PPOLs-80 at Co *K*-edge shows a main peak at 1.48 Å (Figure 3b), which can be assigned to the Co-N bond from porphyrin units. Figure 3c shows the EXAFS fitting curve of Co PPOLs-80, giving quantitative structural parameters of Co sites.[21] As shown in Table S1, the coordination number of Cu-N was determined to be around 4, which is consistent with the schematic model illustrated in Figure 3d. Meanwhile, the wavelet transform (WT) plot shows an intensity maximum at 5.36 $Å^{-1}$ for Co-PPOLs-80, corresponding to the Co-N rather than Co-Co bond (Figure 3e–i), further indicating atomically dispersed cobalt.

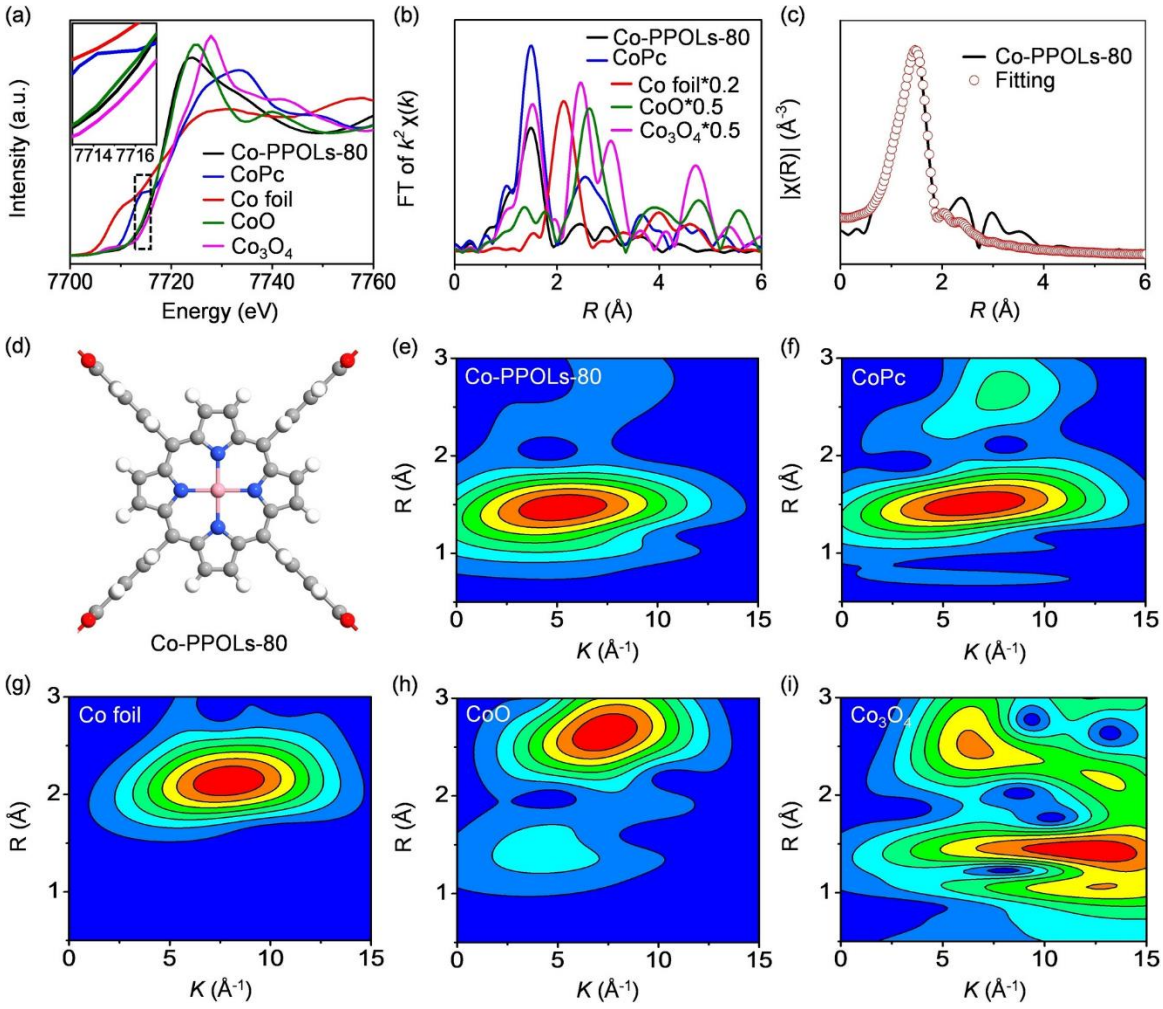

Figure 3 a) Co *K*-edge XANES spectra (inset is the magnified image) and b) FT-EXAFS spectra of Co-PPOLs-80, CoPc, Co foil, CoO, and Co_3O_4. c) EXAFS fitting curve and d) schematic model of Co-PPOLs-80. EXAFS wavelet transforms of e) Co-PPOLs-80, f) CoPc, g) Co foil, h) CoO, and i) Co_3O_4.

To assess our DFT predictions for electrochemical CO_2RR on different M-PPOLs, Ni- and Fe-PPOLs-80 were also synthesized via the same method using $Ni(NO_3)_2{\cdot}6\,H_2O$ and $Fe(NO_3)_3{\cdot}9\,H_2O$ as the metal precursor, respectively. The successful formation of 2D nanolayer morphology and chemical composition were confirmed by TEM, X-ray photoelectron spectroscopy (XPS), Fourier-transform infrared (FTIR), and Raman spectroscopies (Figure S2–S5). The electrochemical CO_2RR activities of all M-PPOLs catalysts were evaluated in a CO_2-saturated 0.1 M $KHCO_3$ electrolyte in an H-type electrochemical cell. As observed in the linear sweep voltammetry (LSV) analysis (Figure 4a) and the current density vs. time (*I*–*t*) plots (Figure 4b), the Co-PPOLs-80 catalyst exhibits significantly higher current density compared with Ni-PPOLs-80 and Fe-PPOLs-80 at the same potential, indicating an optimal electrocatalytic activity. For Co-PPOLs-80, the current density increases gradually from 5.25 to 12.9 mA m^{-2}, when the applied cathodic potential increases from −0.8 to −1.2 V (vs. RHE). Measured by gas chromatography (GC) and nuclear magnetic resonance (NMR), CO_2 molecules were found successfully reduced to gaseous CO (Figure S6), and no liquid products were detected. Meanwhile, isotope-labeled carbon dioxide ($^{13}CO_2$) was further conducted to ensure the generation of CO originated from the gaseous CO_2 in the system (Figure S7). As observed in Figure 4c, the CO_2-to-CO conversion dominates over the hydrogen evolution reaction (HER) over Co-PPOLs-80 across all the investigated potentials, which can be further confirmed by LSV curves under CO_2- and N_2- atmosphere (Figure S8). For example, the FE_{CO} reaches above 80 % at the potential of −0.8 V (vs. RHE), which can be further improved to the maximum value of 94.2 % at −0.9 V (vs. RHE). When the applied cathodic potential goes more negative, the FE_{CO} value gradually decreases, which might be due to the limited CO_2 mass transport at higher current densities. In comparison, the electrochemical CO_2RR activities of Ni-PPOLs-80 and Fe-PPOLs-80 were also examined, which both present lower FE_{CO} compared to that of Co-PPOLs-80 across all the investigated potentials. Meanwhile, the energy efficiency of the CO product (EE_{CO}) was calculated to further evaluate the electrocatalytic activity of the Co-PPOLs-80 catalyst for CO_2RR. As shown in Figure 4d, the Co-PPOLs-80 catalyst shows a maximum EE_{CO} value (59.6 %) at −0.9 V (vs. RHE), which is higher than that of Ni-PPOLs-80 (54.6 %) and Fe-PPOLs-80 (49.1 %). Therefore, Co-PPOLs-80 stands out as the optimal catalyst for CO_2 conversion to generate CO among different M-PPOLs catalysts.

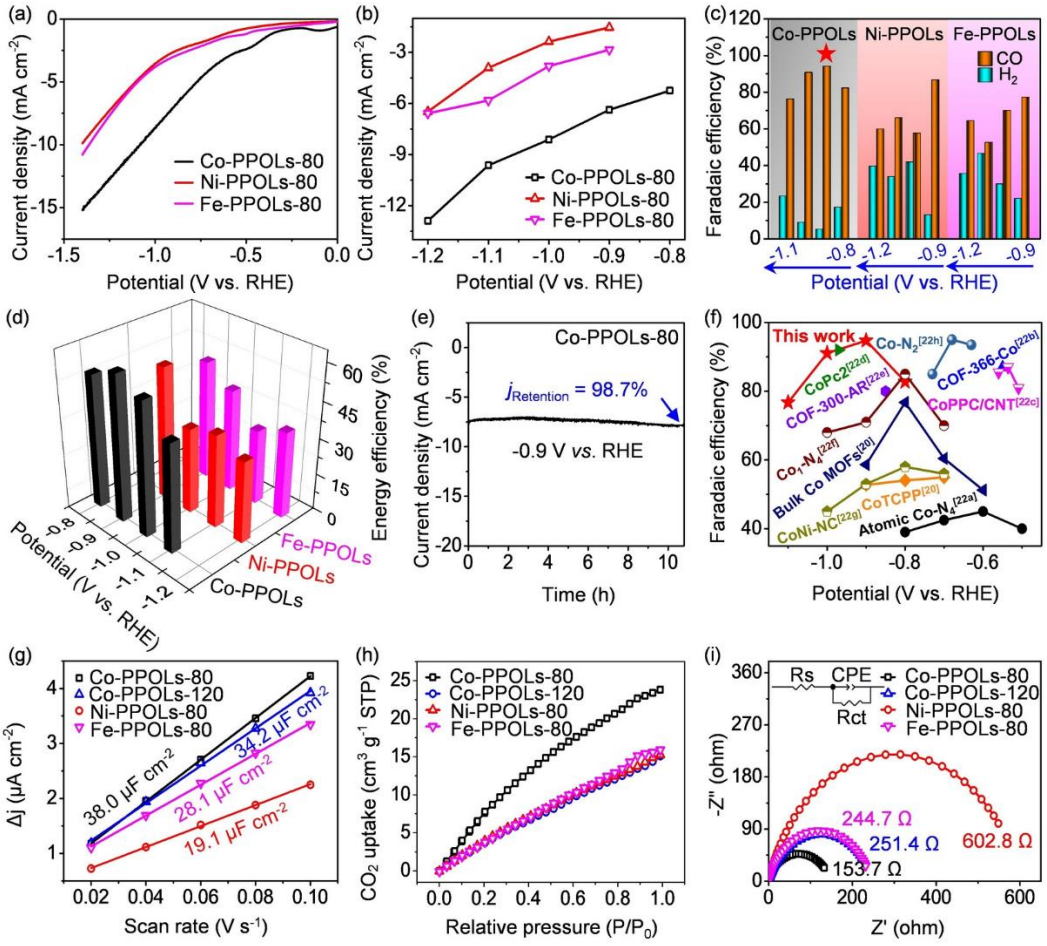

Figure 4 a) LSV curves of M-PPOLs recorded in CO_2-saturated 0.1 M $KHCO_3$ aqueous solution. b) Current density and c) Faradaic efficiencies of CO and H_2 of M-PPOLs at different applied cathodic potentials in electrochemical CO_2RR. d) Energy efficiencies of CO of M-PPOLs at different cathodic potentials. e) Durability test of Co-PPOLs-80 in electrochemical CO_2RR. f) Performance comparisons of Co-PPOLs-80 with other representative Co-based electrocatalysts toward electrochemical CO_2-to-CO conversion.[20, 22] g) The curves of capacitive current density (Δj) against scan rate, h) CO_2 adsorption curves, and i) Nyquist plots of M-PPOLs.

Besides catalytic activity and selectivity, stability is another important factor to evaluate the electrocatalytic performance of a catalyst. The long-term catalytic durability of Co-PPOLs-80 was evaluated at the potential of −0.9 V (vs. RHE) for CO_2RR (Figure 4e), which shows no obvious change in the current density over 10 h electrolysis. Moreover, characterizations of the used Co-PPOLs after long-term stability test by (high-resolution) TEM and XPS evidenced the well-maintained nanolayer structure, metal dispersion, and chemical compositions (Figure S9), further confirming the good durability of Co-PPOLs-80. Note that the reported FE_{CO} is among the best in comparison with the other representative Co-based catalysts for electrochemical CO_2-to-CO conversion (Figure 4f and Table S2).[20, 22] To explore the effects of atomic layer number upon the selectivity

and activity of electrochemical CO_2RR, higher layer number Co-PPOL-120 nanolayers were also obtained by increasing the solvothermal temperature to 120 °C, presenting a much thicker average thickness of ≈5.0 nm (Figure S10). The physicochemical properties of Co-PPOLs were characterized and summarized in Figure S11. As shown in Figure S12, Co-PPOLs-120 exhibits relatively high CO_2 reduction ability at certain potentials, with a peak FE_{CO} of 90.7 % at −1.0 V (vs. RHE). Nevertheless, a higher overpotential is required to achieve the optimal FE_{CO}, which is inferior to that of thinner Co-PPOLs-80 nanolayers.

To further reveal the inherent origins of the superiority of Co-PPOLs-80 for CO_2RR, the electrochemical properties and CO_2 adsorption capacities of different M-PPOLs were analyzed. As shown in Figure 4g and S13, Co-PPOLs-80 exhibits the highest electrochemical surface area (ECSA) according to the double-layer capacitance (C_{dl}) results from cyclic voltammograms, indicating the largest number of active sites. Moreover, the N_2 adsorption-desorption isotherms and the pore-size distributions indicate that Co-PPOLs-80 possesses the largest specific surface area and the highest amount of micropores (Figure S14). In addition, Co-PPOLs-80 shows the strongest CO_2 adsorption ability and high structural stability (Figure 4h, and S15), which is advantageous for CO_2RR. According to the Nyquist plots (Figure 4i), Co-PPOLs-80 exhibits the lowest interfacial electron transfer resistance (R_{ct}), which is conducive to the occurrence of an electrocatalytic process. These results prove that the ultrathin nanostructure of Co-PPOLs-80 ensures the exposure of an abundant number of active sites, thus facilitating the reactant/intermediate adsorption, activation, and conversion.

Since mass transfer would significantly limit the current in the H-type cell, MEA device was further assembled to evaluate the CO_2RR performance of the Co-PPOLs under industrial-relevant current. As shown in Figure 5a, the Co-PPOLs catalyst was used for CO_2 electrolysis in a two-electrode membrane cell device, which was composed of a cathode, an anode, and a polymer electrolyte membrane. The catalysts were brushed onto the two sides of the gas-diffusion electrode, and then pressed to sandwich the membrane. The membrane plays a vital role in the MEA reactor, which performs high electrical conductivity, catalytic activity, and chemical stability. Accordingly, in KOH electrolyte, the current can reach >200 mA at the full-cell voltage of 2.9 V in a two-electrode system (Figure 5b). Meanwhile, faradaic efficiencies of products were calculated under different cell potentials, and the maximum FE_{CO} of 92 % could be achieved at a cell voltage of 2.7 V (Figure 5c). To ensure the long-term durability of Co-PPOLs under industrial conditions, the time-dependent current curve was recorded (Figure 5d) without flushing the electrode or refreshing the electrolyte in the MEA device. The Co-PPOLs could maintain a high FE_{CO} of over 90 % with a stable current up to 180 mA for 20 h.

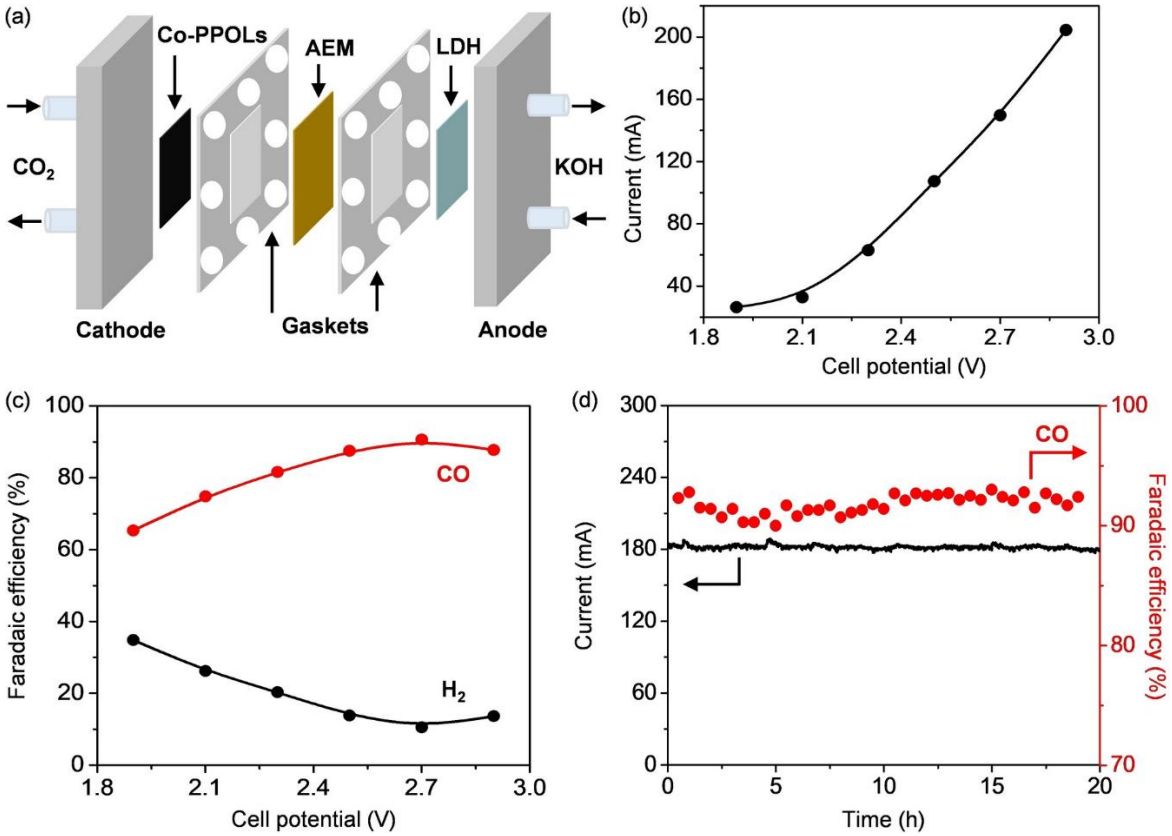

Figure 5 a) Schematic illustration of the MEA device. b) Currents and c) FE_{CO} of Co-PPOLs measured in the MEA device under different cell potentials. d) Long-term stability of Co-PPOLs in the MEA device.

Conclusion

In summary, this study reports the synthesis of 2D self-assembled Co-PPOLs through a facile surfactant-assisted bottom-up synthetic method. The DFT calculations predict that the PPOLs with Co-N_4 catalytic centers can exhibit the optimum activity for electrochemical CO_2-to-CO conversion compared to that of Ni-N_4 and Fe-N_4 sites, which is due to the lowest *CO adsorption energy at Co-N_4 sites that contributes to the rapid *CO desorption and CO formation. The theoretical predictions have been well-assessed by experimental investigations, which demonstrate the optimal CO_2RR activity over Co-PPOLs. The integrated characterizations reveal that the ultrathin Co-PPOLs possess abundant well-defined Co-N_4 sites, highly-ordered structural homogeneity, high specific surface area, enhanced electrical conductivity, and improved CO_2 adsorption capacity, which collectively results in excellent activity and selectivity for CO_2 reduction to CO. The optimal FE_{CO} value achieves up to 94.2 % at a moderate potential of −0.9 V (vs. RHE), accompanied by long-term stability over 10-h. Additionally, industrial-level current can be reached above 200 mA in the MEA device, with the maximum FE_{CO} over 90 % up to 20 h. This work highlights the potential of designing non-noble metal-based porphyrin porous organic frameworks for commercial-scale CO_2 electroreduction.

Acknowledgments

This work was supported by the National Natural Science Foundation of China (22205113, 22202105), the Natural Science Foundation of Jiangsu Province (BK20210626, BK20210608), the Natural Science Foundation of Jiangsu Higher Education Institutions of China (21KJB150027, 21KJA150003), and the China Postdoctoral Science Foundation (2022M711645). Z. Chen acknowledges the support from the Alexander von Humboldt Foundation.

References

1, 1aW. Zhou, K. Cheng, J. C. Kang, C. Zhou, V. Subramanian, Q. H. Zhang, Y. Wang, Chem. Soc. Rev. 2019, 48, 3193–3228; 1bJ. Qiao, Y. Liu, F. Hong, J. J. Zhang, Chem. Soc. Rev. 2014, 43, 631–675; 1cT. Zheng, K. Jiang, H. Wang, Adv. Mater. 2018, 30, 1802066.

2, 2aA. S. Varela, W. Ju, A. Bagger, P. Franco, J. Rossmeisl, P. Strasser, ACS Catal. 2019, 9, 7270–7284; 2bY. Peng, B. Lu, S. Chen, Adv. Mater. 2018, 30, 1801995; 2cH. B. Yang, S. F. Hung, S. Liu, K. Yuan, S. Miao, L. Zhang, X. Huang, H. Wang, W. Cai, R. Chen, J. Gao, X. Yang, W. Chen, Y. Huang, H. M. Chen, C. M. Li, T. Zhang, B. Liu, Nat. Energy 2018, 3, 140–147.

3, 3aZ. Liang, C. Qu, D. Xia, R. Zou, Q. Xu, Angew. Chem. Int. Ed. 2018, 57, 9604–9633; 3bY. S. Wei, M. Zhang, R. Zou, Q. Xu, Chem. Rev. 2020, 120, 12089–12174

4, B. He, Q. Zhang, Z. Pan, L. Li, C. Li, Y. Ling, Z. Wang, M. Chen, Z. Wang, Y. Yao, Q. Li, L. Sun, J. Wang, L. Wei, Chem. Rev. 2022, 122, 10087–10125.

5, G. A. Olah, G. K. Prakash, A. Goeppert, J. Am. Chem. Soc. 2011, 133, 12881–12898.

6, 6aD. Zhao, D. J. Timmons, D. Yuan, H. C. Zhou, Acc. Chem. Res. 2011, 44, 123–133; 6bY. B. Huang, J. Liang, X. S. Wang, R. Cao, Chem. Soc. Rev. 2017, 46, 126–157.

7, J. Shen, R. Kortlever, R. Kas, Y. Y. Birdja, O. Diaz-Morales, Y. Kwon, I. Ledezma-Yanez, K. J. P. Schouten, G. Mul, M. T. M. Koper, Nat. Commun. 2015, 6, 8177.

8, S. Lin, C. S. Diercks, Y. Zhang, N. Kornienko, E. M. Nichols, Y. Zhao, A. R. Paris, D. Kim, P. Yang, O. M. Yaghi, C. J. Chang, Science 2015, 349, 1208–1213.

9, C. Costentin, S. Drouet, M. Robert, J. Savéant, Science 2012, 338, 90–94.

10, H. Zhong, K. H. Ly, M. Wang, Y. Krupskaya, X. Han, J. Zhang, J. Zhang, V. Kataev, B. Buchner, I. M. Weidinger, S. Kaskel, P. Liu, M. Chen, R. Dong, X. Feng, Angew. Chem. Int. Ed. 2019, 58, 10677–10682.

11, D. Chen, H. Feng, J. Li, Chem. Rev. 2012, 112, 6027–6053.

12, M. Naguib, V. N. Mochalin, M. W. Barsoum, Y. Gogotsi, Adv. Mater. 2014, 26, 992–1005.

13, Q. Fu, X. Bao, Chem. Soc. Rev. 2017, 46, 1842–1874.

14, P. T. Hammond, Adv. Mater. 2004, 16, 1271–1293.

15, H. Liu, H. Wang, Q. Song, K. Küster, U. Starke, P. A. van Aken, E. Klemm, Angew. Chem. Int. Ed. 2022, 61, e202117058.

16, R. Yerushalmi, A. Scherz, M. E. V. D. Boom, J. Am. Chem. Soc. 2004, 126, 2700–2701.

17, 17aM. Zhao, Y. Wang, Q. Ma, Y. Huang, X. Zhang, J. Ping, Z. Zhang, Q. Lu, Y. Yu, H. Xu, Y. Zhao, H. Zhang, Adv. Mater. 2015, 27, 7372–7378; 17bM. Zhao, Q. Lu, Q. Ma, H. Zhang, Small Methods 2017, 1, 1600030; 17cE. Choi, C. A. Wray, C. Hu, W. Choe, CrystEngComm 2009, 11, 553–555.

18, 8aZ. Zhang, J. Xiao, X. J. Chen, S. Yu, L. Yu, R. Si, Y. Wang, S. Wang, X. Meng, Y. Wang, Z. Q. Tian, D. Deng, Angew. Chem. Int. Ed. 2018, 57, 16339–16342; 18bL. Sun, Z. Huang, V. Reddu, Angew. Chem. Int. Ed. 2020, 59, 17104–17109.

19, 9aS. R. Ahrenholtz, C. C. Epley, A. J. Morris, J. Am. Chem. Soc. 2014, 136, 2464–2472; 19bN. Kornienko, Y. Zhao, C. S. Kley, C. Zhu, D. Kim, S. Lin, C. J. Chang, O. M. Yaghi, P. Yang, J. Am. Chem. Soc. 2015, 137, 14129–14135; 19cT. He, C. Yang, Y. Chen, N. Huang, S. Duan, Z. Zhang, W. Hu, D. Jiang, Adv. Mater. 2022, 34, 2205186; 19dS. Liu, H. B. Yang, S. F. Hung, J. Ding, W. Z. Cai, L. H. Liu, J. J. Gao, X. Li, X. Ren, Z. Kuang, Y. Huang, T. Zhang, B. Liu, Angew. Chem. Int. Ed. 2020, 59, 798–803.

20, W. Zhang, Y. Xia, S. Chen, Y. Hu, S. Yang, Z. Tie, Z. Jin, Nano Lett. 2022, 22, 3340–3348.

21, 21aH. Qi, J. Yang, F. Liu, L. Zhang, J. Yang, X. Liu, L. Li, Y. Su, Y. Liu, R. Hao, A. Wang, T. Zhang, Nat. Commun. 2021, 12, 3295; 21bW. Liu, Y. Chen, H. Qi, L. Zhang, W. Yan, X. Liu, X. Yang, S. Miao, W. Wang, C. Liu, A. Wang, J. Li, T. Zhang, Angew. Chem. Int. Ed. 2018, 57, 7071–7075.

22, 22aF. Pan, H. Zhang, K. Liu, D. Cullen, K. More, M. Wang, Z. Feng, G. Wang, G. Wu, Y. Li, ACS Catal. 2018, 8, 3116–3122; 22bC. S. Diercks, S. Lin, N. Kornienko, E. A. Kapustin, E. M. Nichols, C. Zhu, Y. Zhao, C. J. Chang, O. M. Yaghi, J. Am. Chem. Soc. 2018, 140, 1116–1122; 22cN. Han, Y. Wang, L. Ma, J. Wen, J. Li, H. Zheng, K. Nie, X. Wang, F. Zhao, Y. Li, J. Fan, J. Zhong, T. Wu, D. J. Miller, J. Lu, S. T. Lee, Y. Li, Chem 2017, 3, 652–664; 22dM. Wang, K. Torbensen, D. Salvatore, S. Ren, D. Joulie, F. Dumoulin, D. Mendoza, B. Lassalle-Kaiser, U. Isci, C. P. Berlinguette, M. Robert, Nat. Commun. 2019, 10, 3602; 22eH. Liu, J. Chu, Z. Yin, X. Cai, L. Zhuang, H. Deng, Chem 2018, 4, 1696–1709; 22fZ. Geng, Y. Cao, W. Chen, X. Kong, Y. Liu, T. Yao, Y. Lin, Appl. Catal. B 2019, 240, 234–240; 22gQ. He, D. Liu, J. H. Lee, Y. Liu, Z. Xie, S. Hwang, S. Kattel, L. Song, J. G. Chen, Angew. Chem. Int. Ed. 2020, 59, 3033–3037; 22hX. Wang, Z. Chen, X. Zhao, T. Yao, W. Chen, R. You, C. Zhao, G. Wu, J. Wang, W. Huang, J. Yang, X. Hong, S. Wei, Y. Wu, Y. Li, Angew. Chem. Int. Ed. 2018, 57, 1944–1948.